

AN FFT-ACCELERATED FDTD SCHEME WITH EXACT ABSORBING CONDITIONS FOR CHARACTERIZING AXIALLY SYMMETRIC RESONANT STRUCTURES

K. Sirenko

King Abdullah University of Science and Technology (KAUST)
KAUST 4700, Thuwal, 23955-6900, Saudi Arabia

V. Pazynin and Y. Sirenko

Institute of Radiophysics and Electronics of National Academy of Sciences of Ukraine (IRE NASU)
12 Acad. Proskura str., Kharkiv, 61085, Ukraine

H. Bagci

King Abdullah University of Science and Technology (KAUST)
KAUST 4700, Thuwal, 23955-6900, Saudi Arabia

Abstract—An accurate and efficient finite-difference time-domain (FDTD) method for characterizing transient waves interactions on axially symmetric structures is presented. The method achieves its accuracy and efficiency by employing localized and/or fast Fourier transform (FFT) accelerated exact absorbing conditions (EACs). The paper details the derivation of the EACs, discusses their implementation and discretization in an FDTD method, and proposes utilization of a blocked-FFT based algorithm for accelerating the computation of temporal convolutions present in nonlocal EACs. The proposed method allows transient analyses to be carried for long time intervals without any loss of accuracy and provides reliable numerical data pertinent to physical processes under resonant conditions. This renders the method highly useful in characterization of high-Q microwave radiators and energy compressors. Numerical results that demonstrate the accuracy and efficiency of the method are presented.

1. INTRODUCTION

Simulation tools capable of accurate and efficient characterization of wave interactions on resonant structures are indispensable during the design of high-Q microwave radiators and energy compressors with storage units and switches [1–3]. Mathematical modeling of wave interactions on these structures gives rise to open initial-boundary value problems. For solving such problems, time-domain simulators might be considered more advantageous over their frequency-domain counterparts since they allow real-time observation of the physical phenomena, can easily incorporate nonlinear components, and provide immediately broadband system response. On the other hand, they typically require long simulation times due to the presence of slowly decaying fields oscillating at resonance frequencies. This renders the transient simulation inefficient and most likely inaccurate because of the error build up during long time marching. In this paper, a finite-difference time-domain (FDTD) method that maintains its accuracy and efficiency even for long simulation times is presented.

FDTD methods are widely preferred in electromagnetic simulation for analyzing transient wave interactions mostly because of the simplicity of their implementation [4]. However, the need for truncation of unbounded computation domains limits their accuracy and efficiency. In this paper, this fundamental drawback is addressed in a fast Fourier transform (FFT) accelerated two-dimensional (2-D) FDTD implementation that employs exact absorbing conditions (EACs).

The problem of accurately truncating unbounded computation domains arose soon after the introduction of FDTD methods. The most well known solutions to this problem include enforcing absorbing boundary conditions on the boundaries of the computation domain and wrapping the computation domain with layers of specially designed absorbing/lossy material, so called perfectly matched layers (PMLs) [4]. Although PMLs are error-controllable (up to certain degree), they will still result in non-negligible errors especially during the simulation of long-duration processes involving resonant structures [4]. In such cases, computation domains can be truncated more accurately using EACs. Several different approaches have been proposed to this end: Dirichlet-to-Neumann maps [5,6], Kirchhoff's integral expressions [7–9], and Fourier transform/eigenfunction expansion method [10,11]. Unfortunately, all of these approaches produce EACs that are nonlocal in space and time, and hence require substantial computational resources. Techniques that localize either time or space interactions have been proposed. However,

these techniques typically contain approximations [6, 12, 13] and hence the computational errors in the solution might be unpredictable especially when the observation time is large.

In this paper, a 2-D FDTD method for transient analysis of axially symmetric structures is presented. The computation domain is truncated using the EACs derived from the radiation conditions for the outgoing modes' spatio-temporal amplitudes [14, 15]. The nonlocal EACs on the planar boundaries located inside the waveguides are localized without the loss of mathematical exactness. In situations, where the localization becomes inefficient, the nonlocal EACs are employed together with a blocked-FFT based algorithm, which is used for accelerating the pertinent (nonlocal) temporal convolutions [16–22]. In addition, the same FFT-based acceleration method is used for computing the convolutions of nonlocal EACs enforced on spherical boundaries, which are located external to the structures only on their radiating ends. To briefly summarize, the contributions of this paper are threefold: (i) A detailed derivation of the (planar and spherical) EACs for axially symmetric waveguide and radiating structures, which follows the approach developed in [14, 15], is presented. (ii) Implementation and discretization of these (local and nonlocal) EACs in an FDTD method are discussed. (iii) Computation of the temporal convolutions present in nonlocal EACs is accelerated using a blocked-FFT based algorithm [16–22].

It should be noted here that the proposed method allows the transient analysis to be carried for long time intervals and can provide highly accurate and reliable numerical data pertinent to physical processes under resonant conditions [14, 23–25]. The proposed method is especially useful for accurate analysis of long-duration processes in resonant radiators and energy compressors with different types of storage units (e.g., waveguide and open resonators with metal, semitransparent, and frequency-selective mirrors) and switches (e.g., distributed grating-type switches, interference and resonant switches).

The remainder of this paper is organized as follows. Section 2 starts with description of the mathematical model for the structures that can be characterized with the proposed method, develops the EACs and details their localization, and ends with the description of the finite-difference based discretization of the EACs and the FFT-based acceleration scheme. Section 3 presents several numerical results that demonstrate the accuracy and efficiency of the proposed method. Section 4 presents conclusions and future research directions.

2. FORMULATION

In this section the mathematical model describing the transient wave interactions on axially symmetric radiators and waveguide units is derived and presented in detail. Section 2.1 presents the descriptions of the model structures and the equations pertinent to TE_{0n} and TM_{0n} waves with axial symmetry. In Section 2.2, the EACs are derived for waveguide units and radiators using the mode expansion of the solutions in the regions external to these structures. This is followed by the localization of EACs for waveguide units. Section 2.3 details the FDTD implementation and FFT-based acceleration technique for computing the temporal convolutions present in nonlocal EACs.

2.1. Mathematical Model

Consider an example waveguide unit and an example radiator with infinite flange presented in Figs. 1(a) and (b), respectively. Here $\mathbf{Q} = \mathbf{Q}_L \cup (\mathbf{I} \cup \mathbf{II} \cup \mathbf{L}_1 \cup \mathbf{L}_2)$ represents the unbounded physical domain; $\mathbf{I} = \{g = \{\rho, z\} \in \mathbf{Q} : b_1 \leq \rho \leq a_1, z < -L_1\}$ represents the infinite regular feeding waveguide, $\mathbf{II} = \{g = \{\rho, z\} \in \mathbf{Q} : b_2 \leq \rho \leq a_2, z > L_2\}$ for Fig. 1(a) and $\mathbf{II} = \{g = \{r, \vartheta\} \in \mathbf{Q} : r > L_2\}$ for Fig. 1(b) represents the homogeneous external region; the remaining bounded computation domain is denoted with \mathbf{Q}_L . $\mathbf{L}_1 = \{g = \{\rho, z\} \in \mathbf{Q} : z = -L_1\}$ represents the virtual boundary between \mathbf{I} and \mathbf{Q}_L and $\mathbf{L}_2 = \{g = \{\rho, z\} \in \mathbf{Q} : z = L_2\}$ for Fig. 1(a) and $\mathbf{L}_2 = \{g = \{r, \vartheta\} \in \mathbf{Q} : r = L_2\}$ for Fig. 1(b) represents the virtual boundary between \mathbf{Q}_L and \mathbf{II} . Conducting and dielectric scatterers with conductivity $\sigma(g, t)$ and relative permittivity $\varepsilon_r(g)$ are assumed to be located in \mathbf{Q}_L . $\sigma(g, t)$ and $\varepsilon_r(g)$ are piecewise constant functions of spatial coordinates $g = \{\rho, z\}$, and the conductivity's time dependence is utilized to simulate changes in a mode of operation. The medium is nonmagnetic, i.e., its relative permeability $\mu_r(g) = 1$. The surface of the perfect electrically conducting parts of the waveguide unit and the radiator is represented by \mathbf{S} and the surface of scatterers located in \mathbf{Q}_L is represented by $\mathbf{S}^{\varepsilon, \sigma}$. \mathbf{S} and $\mathbf{S}^{\varepsilon, \sigma}$ are assumed to be sufficiently smooth. Supports of the source functions $\varphi(g)$ and $\psi(g)$ are assumed to be located in \mathbf{I} ; $\varphi(g)$ and $\psi(g)$ give rise to an incident wave $U^i(g, t)$, which arrives upon the virtual boundary \mathbf{L}_1 at time $t > 0$.

TE_{0n} and TM_{0n} waves propagating in the axially symmetric waveguide unit and radiating to the outside satisfy [14, 15]:

$$\begin{aligned} [-\varepsilon_r(g) \partial_t^2 - P + \partial_z^2 + \partial_\rho(\rho^{-1} \partial_\rho \rho)] U(g, t) &= 0, \quad t > 0, \quad g = \{\rho, z\} \in \mathbf{Q} \\ U(g, 0) = \varphi(g), \quad \partial_t U(g, t)|_{t=0} &= \psi(g), \quad g \in \mathbf{I} \\ E_{tg}(g, t) = 0, \quad g \in \mathbf{S}; \quad U(0, z, t) &= 0, \quad t \geq 0. \end{aligned} \quad (1)$$

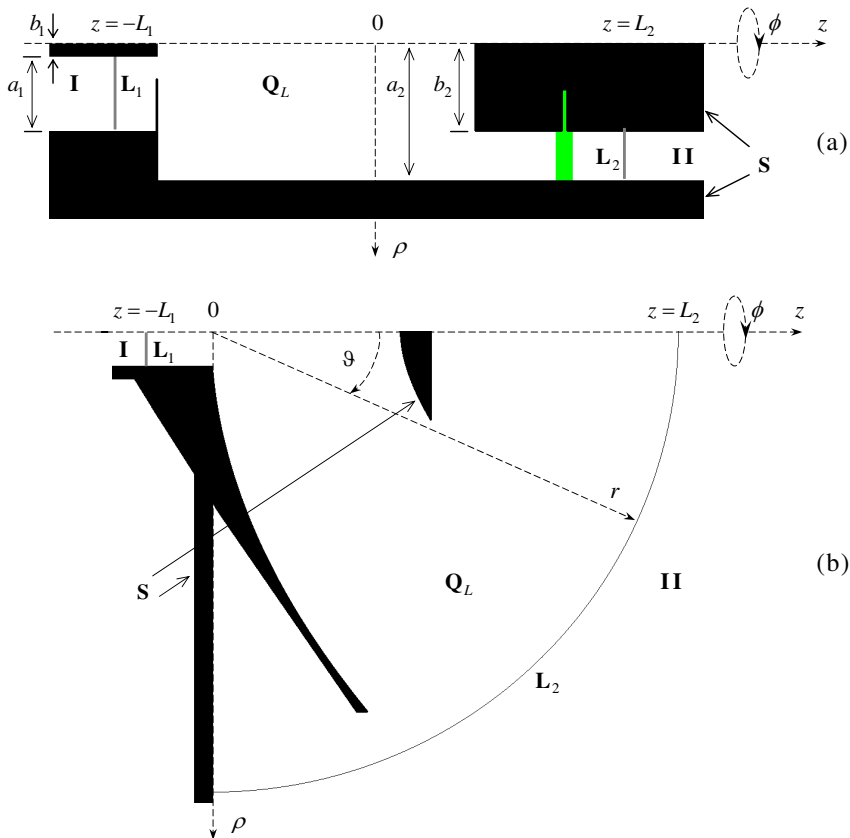


Figure 1. Geometry of the model problems: (a) a waveguide cavity resonator fed and terminated by coaxial waveguides; (b) a parabolic radiator with elliptical subreflector and infinite flange.

Here $U = E_\phi$, $E_\rho = E_z = H_\phi = 0$, $P[U] = \partial_t [\sigma(g, t)U(g, t)]$ for TE_{0n} waves, and $U = H_\phi$, $H_\rho = H_z = E_\phi = 0$, $P[U] = \sigma(g, t) \partial_t U(g, t)$ for TM_{0n} waves. $E_{tg}(g, t)$ is the component of the electric field that is tangential to \mathbf{S} . The SI system is used for all physical parameters except time t which is measured in meters — it is a product of the natural time and the speed of light in free space.

2.2. Derivation of EACs and Their Localization

The unbounded physical domain \mathbf{Q} is reduced to the bounded computation domain \mathbf{Q}_L by defining EACs on the virtual boundaries \mathbf{L}_1 and \mathbf{L}_2 . The EACs are derived from solutions of (1) in homogeneous

external regions **I** and **II** assuming the sources are set to zero (i.e., assuming (1) is a homogenous equation). The following summarizes the steps carried out in this process, which is presented in detail afterwards:

- i. The unknown solutions of homogeneous (1) in **I** and **II** are represented as a product of transverse functions and spatio-temporal amplitudes (using separation of variables). This facilitates the derivation of the EACs as the transverse functions are known (hence, only the spatio-temporal amplitudes should be found) and decouples time and transverse space variables.
- ii. The spatio-temporal amplitudes are obtained as the solutions of pertinent homogeneous initial value problems, which are derived by inserting the “separation of variables” expansion in (i) into homogenous (1)). These solutions are obtained using a standard technique: First, the homogeneous problem is converted into the nonhomogeneous Cauchy problem using the Fourier transform. Then, in the space of generalized functions, the solution of the (generalized) Cauchy problem is obtained by convolving the fundamental solution of the corresponding operator with the right hand side of the problem. Here the right hand side of the problem involves the spatial derivatives of the spatio-temporal amplitudes.
- iii. Inverse Fourier transform provides the solutions of the homogeneous initial value problems in the form of a relation between boundary values of the spatio-temporal amplitudes and their spatial derivatives. These relations are then used as boundary conditions on the virtual boundaries \mathbf{L}_1 and \mathbf{L}_2 . Since the boundary conditions are obtained by the use of rigorous mathematical operations, it is appropriate to name them “exact”. The boundary conditions are called “absorbing” because the wave arriving onto \mathbf{L}_1 and \mathbf{L}_2 from the computation domain \mathbf{Q}_L is neither deformed by the boundaries, nor reflected back as if the wave is being totally absorbed by the external domains **I** and **II** or by the virtual boundaries \mathbf{L}_1 and \mathbf{L}_2 .
- iv. The EACs, which are obtained via the above process, are nonlocal in space and time; therefore, their numerical implementation requires substantial memory and computational resources. This problem is alleviated by localizing the EACs (for waveguide units only). The localization is based on conversion of integral forms into equivalent differential ones.

2.2.1. Separation of Variables and Mode Expansion of the Solution in Homogeneous Domain

If all the requirements of one-valued solvability of the problem (1) in Sobolev space are met [14, 26], then under the aforesaid conditions, the solution of (1) in \mathbf{I} can be written as a sum of incident and scattered fields: $U(g, t) = U^i(g, t) + U_1^s(g, t)$. Separation of variables is applied to $U^i(g, t)$, $U_1^s(g, t)$ and $U(g, t)$ separately and the fields are represented as infinite sums of modes [14]:

$$U^i(g, t) = \sum_n v_{n1}(z, t) \mu_{n1}(\rho), \quad g = \{\rho, z\} \in \mathbf{I} \quad (2a)$$

$$U_1^s(g, t) = \sum_n u_{n1}(z, t) \mu_{n1}(\rho), \quad g = \{\rho, z\} \in \mathbf{I}. \quad (2b)$$

$$U(g, t) = \sum_n u_{n1}^t(z, t) \mu_{n1}(\rho), \quad g = \{\rho, z\} \in \mathbf{I}. \quad (2c)$$

The spatio-temporal (mode) amplitudes $u_{n1}(z, t)$, $v_{n1}(z, t)$ and $u_{n1}^t(z, t)$, and the transverse functions $\mu_{n1}(\rho)$ are related by

$$\left\{ \begin{matrix} u_{n1}(z, t) \\ v_{n1}(z, t) \\ u_{n1}^t(z, t) \end{matrix} \right\} = \int_{b_1}^{a_1} \left\{ \begin{matrix} U_1^s(g, t) \\ U^i(g, t) \\ U(g, t) \end{matrix} \right\} \mu_{n1}(\rho) \rho d\rho, \quad g = \{\rho, z\} \in \mathbf{I}. \quad (3)$$

It should be noted that for $b_1 > 0$ and $b_1 = 0$, \mathbf{I} represents a coaxial and a circular waveguide, respectively. Also, $n \in \{0, 1, 2, \dots\}$ when TM_{0n} waves are considered and \mathbf{I} is a coaxial waveguide, and $n \in \{1, 2, 3, \dots\}$ in all other cases. Inserting (2b) into the homogenous version of (1) (i.e., assuming $\varepsilon_r(g) = 1$, $\sigma(g, t) = 0$, $\varphi(g) = 0$ and $\psi(g) = 0$), equations satisfied by $\mu_{n1}(\rho)$ and $u_{n1}(z, t)$ are obtained (see (4) and (5) below). The transverse functions $\mu_{n1}(\rho)$ and the corresponding eigenvalues λ_{n1} are specified by nontrivial solutions of the homogeneous problem [14, 15]

$$\begin{aligned} & [\partial_\rho (\rho^{-1} \partial_\rho \rho) + \lambda_{n1}^2] \mu_{n1}(\rho) = 0; \quad b_1 < \rho < a_1; \\ TE_{0n}: & \mu_{n1}(b_1) = \mu_{n1}(a_1) = 0 \\ TM_{0n}: & \partial_\rho (\rho \mu_{n1}(\rho))|_{\rho=b_1} = 0 [\mu_{n1}(b_1) = 0 \text{ if } b_1 = 0], \partial_\rho (\rho \mu_{n1}(\rho))|_{\rho=a_1} = 0. \end{aligned} \quad (4)$$

Solutions of (4) are well-known and provided below for TE_{0n} and TM_{0n} waves [14, 15]:

$$\begin{aligned} TE_{0n}: & \\ \mu_{n1}(\rho) &= G_{1,1}(\lambda_{n1}, \rho, b_1) \sqrt{2} [a_1^2 G_{0,1}^2(\lambda_{n1}, a_1, b_1) - b_1^2 G_{0,1}^2(\lambda_{n1}, b_1, b_1)]^{-1/2}, \\ \lambda_{n1} &\in \{\lambda : \lambda > 0, G_{1,1}(\lambda, a_1, b_1) = 0\}, \quad b_1 < \rho < a_1; \\ \mu_{n1}(\rho) &= J_1(\lambda_{n1} \rho) \sqrt{2} [a_1 J_0(\lambda_{n1} a_1)]^{-1}, \\ \lambda_{n1} &\in \{\lambda : \lambda > 0, J_1(\lambda a_1) = 0\} \text{ if } b_1 = 0; \end{aligned}$$

TM_{0n} :

$$\mu_{01}(\rho) = \left[\rho \sqrt{\ln(a_1/b_1)} \right]^{-1}, \quad \lambda_{01} = 0, \quad b_1 < \rho < a_1,$$

$$\mu_{n1}(\rho) = G_{1,0}(\lambda_{n1}, \rho, a_1) \sqrt{2} \left[a_1^2 G_{1,0}^2(\lambda_{n1}, a_1, a_1) - b_1^2 G_{1,0}^2(\lambda_{n1}, b_1, a_1) \right]^{-1/2},$$

$$\lambda_{n1} \in \{ \lambda : \lambda > 0, G_{0,0}(\lambda, b_1, a_1) = 0 \}, \quad n > 0, \quad b_1 < \rho < a_1;$$

$$\mu_{n1}(\rho) = J_1(\lambda_{n1}\rho) \sqrt{2} \left[a_1 J_1(\lambda_{n1}a_1) \right]^{-1},$$

$$\lambda_{n1} \in \{ \lambda : \lambda > 0, J_0(\lambda a_1) = 0 \}, \quad n > 0 \text{ if } b_1 = 0.$$

Here $G_{q,p}(\lambda, \rho, c) = J_q(\lambda\rho)N_p(\lambda c) - N_q(\lambda\rho)J_p(\lambda c)$, $J_q(\cdot)$ and $N_q(\cdot)$ are Bessel and Neumann functions. The spatio-temporal amplitudes $u_{n1}(z, t)$ are solutions of the initial value problem

$$\begin{aligned} [-\partial_t^2 + \partial_z^2 - \lambda_{n1}^2] u_{n1}(z, t) &= 0; t > 0 & ; \quad z \leq -L_1. \\ u_{n1}(z, 0) = 0, \partial_t u_{n1}(z, t)|_{t=0} &= 0 \end{aligned} \quad (5)$$

Similar to the solution of (1) in **I**, the solution of (1) in **II** can also be decomposed using separation of variables. However, in **II** only scattered fields exist, $U(g, t) = U_2^s(g, t)$, (i.e., all sources are assumed to be located in **I**):

$$U_2^s(g, t) = \sum_n u_{n2}(z, t) \mu_{n2}(\rho), \quad g = \{\rho, z\} \in \mathbf{II}, \quad (6a)$$

$$U_2^s(g, t) = \sum_n u_{n2}(r, t) \mu_{n2}(\cos \vartheta), \quad g = \{r, \vartheta\} \in \mathbf{II}. \quad (6b)$$

The spatio-temporal (mode) amplitudes $u_{n2}(z, t)$ and $u_{n2}(r, t)$, and the transverse functions $\mu_{n2}(\rho)$ and $\mu_{n2}(\cos \vartheta)$ are related by

$$u_{n2}(z, t) = \int_{b_2}^{a_2} U(g, t) \mu_{n2}(\rho) \rho d\rho, \quad (7a)$$

$$u_{n2}(r, t) = \int_0^{\pi/2} U(g, t) \mu_{n2}(\cos \vartheta) \sin \vartheta d\vartheta. \quad (7b)$$

For $b_2 > 0$ and $b_2 = 0$, in Fig. 1(a) **II** represents a coaxial and a circular waveguide, respectively. In (6a), $n \in \{0, 1, 2, \dots\}$ when TM_{0n} waves are considered and **II** is a coaxial waveguide, and $n \in \{1, 2, 3, \dots\}$ in all other cases; in (6b) $n \in \{2, 4, 6, \dots\}$ for TE_{0n} waves, and $n \in \{1, 3, 5, \dots\}$ for TM_{0n} waves. It is evident that everything stated above for $\mu_{n1}(\rho)$ and $u_{n1}(z, t)$ remains valid for $\mu_{n2}(\rho)$ and $u_{n2}(z, t)$ as well. Inserting (6b) into the homogenous version of (1), equations satisfied by $u_{n2}(r, t)$ and $\mu_{n2}(\cos \vartheta)$ are obtained (see (8) and (9) below). The transverse functions $\mu_{n2}(\cos \theta)$ and the corresponding

eigenvalues λ_{n2} are specified by nontrivial solutions of the homogenous Sturm-Liouville problem [14]:

$$\begin{aligned} & [\partial_\vartheta^2 + \text{ctg}\vartheta \partial_\vartheta - \sin^{-2} \vartheta + \lambda_{n2}^2] \mu_{n2}(\cos \vartheta) = 0; 0 < \vartheta < \pi/2; \\ TE_{0n} : \mu_{n2}(\cos \vartheta)|_{\vartheta=0, \pi/2} &= 0 \\ TM_{0n} : \mu_{n2}(\cos \vartheta)|_{\vartheta=0} &= \sin^{-1} \vartheta \partial_\vartheta [\mu_{n2}(\cos \vartheta)]|_{\vartheta=\pi/2} = 0. \end{aligned} \tag{8}$$

Solutions of (8) are well-known and provided below for TE_{0n} and TM_{0n} waves [14]:

$$\mu_{n2}(\cos \vartheta) = P_n^1(\cos \vartheta) \sqrt{(2n+1)/(n(n+1))}, \lambda_{n2}^2 = n(n+1).$$

Here, $P_n^1(\cdot)$ are associated Legendre functions of the first kind of degree n . The mode amplitudes $u_{n2}(r, t)$ are solutions of the initial value problem

$$\begin{aligned} [-\partial_t^2 + \partial_r^2 - r^{-2} \lambda_{n2}^2] r u_{n2}(r, t) &= 0; \quad r \geq L_2, t > 0 \\ u_{n2}(r, 0) = \partial_t u_{n2}(r, t)|_{t=0} &= 0; \quad r \geq L_2. \end{aligned} \tag{9}$$

2.2.2. Exact Absorbing Conditions for Waveguide Units and Their Localization

In this section, the derivation of the EACs enforced on the virtual boundaries \mathbf{L}_1 and \mathbf{L}_2 for the solution of (1) in domain \mathbf{Q}_L of compact waveguide units (Fig. 1(a)) is detailed. First, the derivation of the EAC on \mathbf{L}_1 is presented; then the EAC on \mathbf{L}_2 , which is obtained in the same way, is only written down. This is followed by the localization of EACs.

The derivation of the EAC on \mathbf{L}_1 starts with applying the cosine Fourier transform, defined with transform \leftrightarrow inverse transform pair

$$\begin{aligned} \tilde{f}(\omega) = \mathfrak{S}_c[f(\bar{z})] &\equiv \sqrt{\frac{2}{\pi}} \int_0^\infty f(\bar{z}) \cos(\omega \bar{z}) d\bar{z} \leftrightarrow \\ f(\bar{z}) = \mathfrak{S}_c^{-1}[\tilde{f}(\omega)] &\equiv \sqrt{\frac{2}{\pi}} \int_0^\infty \tilde{f}(\omega) \cos(\omega \bar{z}) d\omega, \end{aligned} \tag{10}$$

to (5). This results in the Cauchy problem for the image $\tilde{u}_{n1}(\omega, t) = \mathfrak{S}_c[u_{n1}(\bar{z}, t)]$, $\bar{z} = -(z + L_1)$, $\bar{z} \geq 0$:

$$\begin{aligned} [\partial_t^2 + (\lambda_{n1}^2 + \omega^2)] \tilde{u}_{n1}(\omega, t) &= -\sqrt{2/\pi} \partial_z u_{n1}(\bar{z}, t)|_{\bar{z}=0}; \quad \omega > 0, t > 0 \\ \tilde{u}_{n1}(\omega, 0) = 0, \partial_t \tilde{u}_{n1}(\omega, t)|_{t=0} &= 0; \quad \omega \geq 0 \end{aligned} \tag{11}$$

In the derivation of (11), cosine Fourier transform pair $\mathfrak{S}_c[\partial_{\bar{z}}^2 f(\bar{z})] =$

$-\omega^2 \tilde{f}(\omega) - \sqrt{2/\pi} \partial_{\bar{z}} f(\bar{z})|_{\bar{z}=0}$, is used. It is also assumed that $U_1^s(g, t)$ in domain **I** does not contain any wave components propagating in $+z$ direction, and the wave components propagating in $-z$ direction vanish for sufficiently large $|z|$ at any finite instant of time $t = T$ (because of the finite speed of light).

Problem (11) can be solved analytically using concepts of generalized functions and fundamental solutions [27]. The generalized statement of the problem (11) is obtained carrying out the standard procedure: $\tilde{u}_{n1}(\omega, t)$ and $\partial_z u_{n1}(\bar{z}, t)|_{\bar{z}=0}$ are extended with zeroes on semi-axis $t < 0$ and initial conditions of (11) are embedded into the equation itself. Thus, the generalized statement of the problem (11) reads as [27]

$$[\partial_t^2 + (\lambda_{n1}^2 + \omega^2)] \tilde{u}_{n1}(\omega, t) = -\sqrt{2/\pi} \partial_z u_{n1}(\bar{z}, t)|_{\bar{z}=0} + \delta^{(1)}(t) \tilde{u}_{n1}(\omega, 0) + \delta(t) \partial_t \tilde{u}_{n1}(\omega, t)|_{t=0}; \omega > 0, -\infty < t < \infty.$$

Here $\delta(\cdot)$ is Dirac delta function and $\delta^{(1)}(\cdot)$ is its generalized first derivative. This equation is simplified using the zero initial conditions of (11):

$$D\left(\sqrt{\lambda_{n1}^2 + \omega^2}\right) [\tilde{u}_{n1}(\omega, t)] \equiv [\partial_t^2 + (\lambda_{n1}^2 + \omega^2)] \tilde{u}_{n1}(\omega, t) = -\sqrt{2/\pi} \partial_z u_{n1}(\bar{z}, t)|_{\bar{z}=0}; \omega > 0, -\infty < t < \infty. \tag{12}$$

The fundamental solution of the operator $D(\lambda) \equiv [\partial_t^2 + \lambda^2]$ is known [14]: $G(\lambda, t) = \chi(t)\lambda^{-1} \sin \lambda t$, where $\chi(\cdot)$ is Heaviside step function. The convolution of $G(\lambda, t)$ with the right-hand side of (12) yields the solution of (12) [27]:

$$\tilde{u}_{n1}(\omega, t) = -\sqrt{\frac{2}{\pi}} \int_0^t \sin\left[(t-\tau)\sqrt{\lambda_{n1}^2 + \omega^2}\right] \frac{\partial_z u_{n1}(\bar{z}, \tau)|_{\bar{z}=0}}{\sqrt{\lambda_{n1}^2 + \omega^2}} d\tau; \omega \geq 0, t \geq 0. \tag{13}$$

Applying inverse cosine Fourier transform (10) to (13) and using $z = -(\bar{z} + L_1)$, yields

$$u_{n1}(z, t) = \int_0^{t+z+L_1} J_0\left[\lambda_{n1} \left((t-\tau)^2 - (z+L_1)^2\right)^{1/2}\right] \partial_z u_{n1}(z, \tau)|_{z=-L_1} d\tau, \tag{14}$$

$$z \leq -L_1, t \geq 0.$$

Expression (14) defines a transport operator, which relates the values of spatio-temporal amplitudes' derivatives $\partial_z u_{n1}(z, t)|_{z=-L_1}$ on the virtual boundary \mathbf{L}_1 to the values of amplitudes $u_{n1}(z, t)$ anywhere

in the regular waveguide **I**. In the other words, the transport operator connects the near field to the far field. Thus, it allows the evolution of the transient wave $U_1^s(g, t)$ to be tracked during its propagation along the regular waveguide **I**.

If the observation point in (14) lies on the artificial boundary \mathbf{L}_1 , i.e., $z = -L_1$, then (14) becomes

$$u_{n1}(-L_1, t) = \int_0^t J_0[\lambda_{n1}(t - \tau)] \partial_z u_{n1}(z, \tau)|_{z=-L_1} d\tau; \quad t \geq 0. \quad (15)$$

Using (15), (2b) and (3), taking into account the orthonormality of the transverse functions $\mu_{n1}(\rho)$, and considering the fact that $U(\rho, -L_1, t) = U^i(\rho, -L_1, t) + U_1^s(\rho, -L_1, t)$, one obtains

$$U(\rho, -L_1, t) - U^i(\rho, -L_1, t) = \sum_n \left\{ \int_0^t J_0[\lambda_{n1}(t - \tau)] \times \left[\int_{b_1}^{a_1} \partial_z [U(\tilde{\rho}, z, \tau) - U^i(\tilde{\rho}, z, \tau)]|_{z=-L_1} \mu_{n1}(\tilde{\rho}) \tilde{\rho} d\tilde{\rho} \right] d\tau \right\} \mu_{n1}(\rho);$$

$$b_1 \leq \rho \leq a_1, \quad t \geq 0. \quad (16)$$

Equation (15) establishes a relation between boundary values of the amplitudes and their derivatives; the overall behavior of the wave is governed by (16). Then, (16) can be regarded as an EAC on the virtual boundary \mathbf{L}_1 : the scattered wave $U_1^s(g, t) = U(g, t) - U^i(g, t)$ is neither deformed by the boundary \mathbf{L}_1 , nor reflected back into the domain \mathbf{Q}_L .

Apparently, in order to use condition (16) one needs to know the time dependence of both incident wave $U^i(g, t)$ and its derivative with respect to z on the virtual boundary \mathbf{L}_1 . These two functions cannot be set arbitrary. Appropriate values of the derivative must be in agreement with the values of the function $U^i(g, t)$ and vice versa (principle of causality). A relation between $v_{n1}(-L_1, t)$ and $\partial_z v_{n1}(z, t)|_{z=-L_1}$ is obtained following the same steps used in derivation of (15):

$$v_{n1}(-L_1, t) = - \int_0^t J_0(\lambda_{n1}(t - \tau)) \partial_z v_{n1}(z, \tau)|_{z=-L_1} d\tau; \quad t \geq 0. \quad (17)$$

The EAC on the virtual boundary \mathbf{L}_2 can be derived similarly, when **II** is a waveguide. Therefore the derivation will not be repeated

here but the result is provided as

$$\begin{aligned}
 U(\rho, L_2, t) = & \\
 - \sum_n \left\{ \int_0^t J_0[\lambda_{n2}(t-\tau)] \left[\int_{b_2}^{a_2} \partial_z U(\tilde{\rho}, z, \tau) \Big|_{z=L_2} \mu_{n2}(\tilde{\rho}) \tilde{\rho} d\tilde{\rho} \right] d\tau \right\} \mu_{n2}(\rho); & \\
 b_2 \leq \rho \leq a_2, \quad t \geq 0. & \tag{18}
 \end{aligned}$$

Discretization of the spatially and temporally nonlocal EACs (16) and (18) calls for substantial memory and computational resources as all boundary values of the spatio-temporal amplitudes obtained at all previous time steps must be stored in order to calculate the values of the amplitudes at the next step (note the ranges of integrals over τ and $\tilde{\rho}$ that indicate nonlocality). This problem is alleviated by localizing the EACs as described next.

The localization is achieved by converting the integral forms into differential ones. Taking into account the representation $J_0(x) = (2/\pi) \int_0^{\pi/2} \cos(x \sin \varphi) d\varphi$ [28], (15) is rewritten as

$$\begin{aligned}
 u_{n1}(-L_1, t) = \frac{2}{\pi} \int_0^{\pi/2} \left\{ \int_0^t \cos(\lambda_{n1}(t-\tau) \sin \varphi) \partial_z u_{n1}(z, \tau) \Big|_{z=-L_1} d\tau \right\} d\varphi; & \\
 t \geq 0. & \tag{19}
 \end{aligned}$$

The derivation of the differential form requires the introduction of the variables

$$\begin{aligned}
 w_{n1}(t, \varphi) = \int_0^t \frac{\sin(\lambda_{n1}(t-\tau) \sin \varphi) \partial_z u_{n1}(z, \tau) \Big|_{z=-L_1}}{\lambda_{n1} \sin \varphi} d\tau; & \\
 t \geq 0, \quad 0 \leq \varphi \leq \pi/2, & \tag{20}
 \end{aligned}$$

and

$$W_1(\rho, t, \varphi) = \sum_n w_{n1}(t, \varphi) \mu_{n1}(\rho). \tag{21}$$

Taking the derivative of (20) with respect to t yields

$$\partial_t w_{n1}(t, \varphi) = \int_0^t \cos(\lambda_{n1}(t-\tau) \sin \varphi) \partial_z u_{n1}(z, \tau) \Big|_{z=-L_1} d\tau. \tag{22}$$

Substituting (22) into (19) yields

$$u_{n1}(-L_1, t) = \frac{2}{\pi} \int_0^{\pi/2} \partial_t w_{n1}(t, \varphi) d\varphi; \quad t \geq 0. \tag{23}$$

Integral (20) is equivalent to the solution of differential equation

$$\begin{aligned} [\partial_t^2 + \lambda_{n1}^2 \sin^2 \varphi] w_{n1}(t, \varphi) &= \partial_z u_{n1}(z, t)|_{z=-L_1}; t > 0 \\ w_{n1}(0, \varphi) &= \partial_t w_{n1}(t, \varphi)|_{t=0} = 0 \end{aligned} \tag{24}$$

Indeed, proceeding from (24) to the generalized Cauchy problem [27] and using the fundamental solution $G(\lambda, t) = \chi(t)\lambda^{-1} \sin \lambda t$ of the operator $D(\lambda) \equiv [\partial_t^2 + \lambda^2]$ (see [14]), it becomes clear that both (20) and (24) define the same function $w_{n1}(t, \varphi)$. From the equation in (4), it follows that $w_{n1}(t, \varphi)$, $\mu_{n1}(\rho)$, and $W_1(\rho, t, \varphi)$ satisfy $\sum_n \lambda_{n1}^2 w_{n1}(t, \varphi) \mu_{n1}(\rho) = -\partial_\rho(\rho^{-1} \partial_\rho(\rho W_1(\rho, t, \varphi)))$. Using this relation, (2b), (21), taking into account the orthonormality of the transverse functions $\mu_{n1}(\rho)$, and considering the fact that $U(\rho, -L_1, t) = U^i(\rho, -L_1, t) + U_1^s(\rho, -L_1, t)$ one obtains

$$\begin{aligned} U(\rho, -L_1, t) - U^i(\rho, -L_1, t) &= \frac{2}{\pi} \int_0^{\pi/2} \partial_t W_1(\rho, t, \varphi) d\varphi; t \geq 0, b_1 < \rho < a_1 \\ [\partial_t^2 - \sin^2 \varphi \partial_\rho(\rho^{-1} \partial_\rho \rho)] W_1(\rho, t, \varphi) &= \partial_z [U(\rho, z, t) - U^i(\rho, z, t)]|_{z=-L_1}; b_1 < \rho < a_1, t > 0 \\ W_1(\rho, 0, \varphi) &= \partial_t W_1(\rho, t, \varphi)|_{t=0} = 0; b_1 < \rho < a_1 \\ TE_{0n} : W_1(b_1, t, \varphi) &= W_1(a_1, t, \varphi) = 0 \\ TM_{0n} : \partial_\rho(\rho W_1(\rho, t, \varphi))|_{\rho=b_1} &= 0 [W_1(0, t, \varphi) = 0 \text{ if } b_1 = 0], \\ \partial_\rho(\rho W_1(\rho, t, \varphi))|_{\rho=a_1} &= 0. \end{aligned} \tag{25}$$

Here $W_1(\rho, t, \varphi)$ is the solution of auxiliary initial-boundary value problem in (25), $0 \leq \varphi \leq \pi/2$ is a numerical parameter. Condition (25) is local in space and time and analytical equivalent to EAC (16) on the virtual boundary \mathbf{L}_1 .

The local EAC on the virtual boundary \mathbf{L}_2 is derived similarly:

$$\begin{aligned} U(\rho, L_2, t) &= \frac{2}{\pi} \int_0^{\pi/2} \partial_t W_2(\rho, t, \varphi) d\varphi; t \geq 0, b_2 < \rho < a_2 \\ [\partial_t^2 - \sin^2 \varphi \partial_\rho(\rho^{-1} \partial_\rho \rho)] W_2(\rho, t, \varphi) &= -\partial_z U(\rho, z, t)|_{z=L_2}; \\ b_2 < \rho < a_2, t > 0 \\ W_2(\rho, 0, \varphi) &= \partial_t W_2(\rho, t, \varphi)|_{t=0} = 0; b_2 < \rho < a_2 \\ TE_{0n} : W_2(b_2, t, \varphi) &= W_2(a_2, t, \varphi) = 0 \\ TM_{0n} : \partial_\rho(\rho W_2(\rho, t, \varphi))|_{\rho=b_2} &= 0 [W_2(0, t, \varphi) = 0 \text{ if } b_2 = 0], \\ \partial_\rho(\rho W_2(\rho, t, \varphi))|_{\rho=a_2} &= 0. \end{aligned} \tag{26}$$

2.2.3. Exact Absorbing Conditions for Radiating Structures

In this section, the EAC enforced on the spherical virtual boundary \mathbf{L}_2 for the solution of (1) in the domain \mathbf{Q}_L of radiators with infinite flange (Fig. 1(b)) is detailed.

Before the derivation of the EACs on the spherical virtual boundary \mathbf{L}_2 , the following integral transform is studied:

$$\tilde{f}(\omega) = \int_{L_2}^{\infty} f(r) Z_{\gamma}(\omega, r) dr; \omega \geq 0. \tag{27}$$

Here $Z_{\gamma}(\omega, r) = r^a [\alpha(\omega) J_{\gamma}(\omega r) + \beta(\omega) N_{\gamma}(\omega r)]$ is the kernel, $N_{\gamma}(\cdot)$ are cylindrical Neumann functions, and $a, \gamma, \alpha(\omega)$, and $\beta(\omega)$ are the coefficient to be determined. The kernel $Z_{\gamma}(\omega, r)$ satisfies [28]

$$\left[\partial_r^2 + \frac{1-2a}{r} \partial_r + \omega^2 + \frac{a^2 - \gamma^2}{r^2} \right] Z_{\gamma}(\omega, r) = 0. \tag{28}$$

The following equality is obtained using integration by parts:

$$\begin{aligned} & \int_{L_2}^{\infty} \partial_r^2 w_{n2}(r, t) Z_{\gamma}(\omega, r) dr \\ &= \partial_r w_{n2}(r, t) Z_{\gamma}(\omega, r) |_{L_2}^{\infty} - \int_{L_2}^{\infty} \partial_r w_{n2}(r, t) \partial_r Z_{\gamma}(\omega, r) dr \\ &= \partial_r w_{n2}(r, t) Z_{\gamma}(\omega, r) |_{L_2}^{\infty} - w_{n2}(r, t) \partial_r Z_{\gamma}(\omega, r) |_{L_2}^{\infty} \\ & \quad + \int_{L_2}^{\infty} w_{n2}(r, t) \partial_r^2 Z_{\gamma}(\omega, r) dr \end{aligned} \tag{29}$$

Here $w_{n2}(r, t) = r u_{n2}(r, t)$ is an auxiliary function. From (28) it follows that

$$\begin{aligned} & \int_{L_2}^{\infty} w_{n2}(r, t) \partial_r^2 Z_{\gamma}(\omega, r) dr = \\ & - \int_{L_2}^{\infty} w_{n2}(r, t) \left[\frac{1-2a}{r} \partial_r + \omega^2 + \frac{a^2 - \gamma^2}{r^2} \right] Z_{\gamma}(\omega, r) dr. \end{aligned} \tag{30}$$

Taking into account the fact that functions $w_{n2}(r, t)$ vanish for any finite t and sufficiently large r (because of the finite speed of light),

applying the transform (27) to the equation of problem (9), using (29) and (30), keeping in mind that in (9) $\lambda_{n2}^2 = n(n + 1)$, and setting the kernel's coefficients as $a = 1/2$ and $\gamma = n + 1/2$, one obtains

$$\int_{L_2}^{\infty} [-\partial_t^2 - \omega^2] w_{n2}(r, t) Z_{\gamma}(\omega, r) dr - \partial_r w_{n2}(r, t)|_{r=L_2} Z_{\gamma}(\omega, L_2) + w_{n2}(L_2, t) \partial_r Z_{\gamma}(\omega, r)|_{r=L_2} = 0. \tag{31}$$

From (31) and (27) follows simple differential equation with respect to the unknown images $\tilde{w}_{n2}(\omega, t)$ of the functions $w_{n2}(r, t)$:

$$[\partial_t^2 + \omega^2] \tilde{w}_{n2}(\omega, t) = w_{n2}(L_2, t) \partial_r Z_{\gamma}(\omega, r)|_{r=L_2} - \partial_r w_{n2}(r, t)|_{r=L_2} Z_{\gamma}(\omega, L_2); \quad \omega \geq 0, \quad t > 0 \tag{32}$$

Now coefficients $\alpha(\omega)$ and $\beta(\omega)$ of the kernel $Z_{\gamma}(\omega, r)$ should be defined in such a way that inverse of the transform (27) exists and the resulting EAC is as simple as possible and also convenient in realization. To obtain a simple and realizable EAC, the derivative of function $w_{n2}(r, t)$ with respect to the radial variable r , should be eliminated, as it is difficult to approximate the radial derivative on a curvilinear boundary in rectangular coordinates $\{\rho, z\}$. So, let the coefficient $Z_{\gamma}(\omega, L_2)$, which multiplies $\partial_r w_{n2}(r, t)|_{r=L_2}$ in (32), be identically zero:

$$Z_{\gamma}(\omega, L_2) = \sqrt{L_2} [\alpha(\omega) J_{\gamma}(\omega L_2) + \beta(\omega) N_{\gamma}(\omega L_2)] = 0; \quad \omega \geq 0. \tag{33}$$

The requirement (33) is satisfied when $\alpha(\omega) = -N_{\gamma}(\omega L_2)$ and $\beta(\omega) = J_{\gamma}(\omega L_2)$, which turns (27) into the Weber-Orr transform [29]

$$\tilde{f}(\omega) = \int_{L_2}^{\infty} [J_{\gamma}(\omega L_2) N_{\gamma}(\omega r) - N_{\gamma}(\omega L_2) J_{\gamma}(\omega r)] f(r) \sqrt{r} dr \leftrightarrow f(r) = \sqrt{r} \int_0^{\infty} \frac{J_{\gamma}(\omega L_2) N_{\gamma}(\omega r) - N_{\gamma}(\omega L_2) J_{\gamma}(\omega r)}{J_{\gamma}^2(\omega L_2) + N_{\gamma}^2(\omega L_2)} \tilde{f}(\omega) \omega d\omega \tag{34}$$

The coefficient $\partial_r Z_{\gamma}(\omega, r)|_{r=L_2}$ in the remaining term in the right-hand side of (32) is equal to

$$\begin{aligned} \partial_r Z_{\gamma}(\omega, r)|_{r=L_2} &= \left(2\sqrt{L_2}\right)^{-1} [J_{\gamma}(\omega L_2) N_{\gamma}(\omega L_2) - N_{\gamma}(\omega L_2) J_{\gamma}(\omega L_2)] \\ &+ \omega\sqrt{L_2} [J_{\gamma}(\omega L_2) N'_{\gamma}(\omega L_2) - N_{\gamma}(\omega L_2) J'_{\gamma}(\omega L_2)] \\ &= \omega\sqrt{L_2} W \{J_{\gamma}(\omega L_2), N_{\gamma}(\omega L_2)\} = 2 / \left(\pi\sqrt{L_2}\right) \end{aligned} \tag{35}$$

Here $W \{J_\gamma(\omega L_2), N_\gamma(\omega L_2)\} = 2/(\pi\omega L_2)$ is Wronskian [28]; $N'_\gamma(\omega L_2)$ and $J'_\gamma(\omega L_2)$ are the derivatives of the functions $J_\gamma(\omega L_2)$ and $N_\gamma(\omega L_2)$ with respect to (ωL_2) . From (9), (32), (33) and (35) the following Cauchy problem in the unknown image $\tilde{w}_{n2}(\omega, t)$ is obtained:

$$\begin{aligned}
 & [\partial_t^2 + \omega^2] \tilde{w}_{n2}(\omega, t) = 2 \left(\pi\sqrt{L_2}\right)^{-1} w_{n2}(L_2, t); \quad t > 0, \quad \omega \geq 0. \quad (36) \\
 & \partial_t \tilde{w}_{n2}(\omega, t)|_{t=0} = \tilde{w}_{n2}(\omega, 0) = 0; \quad \omega \geq 0
 \end{aligned}$$

A solution of the problem (36) is obtained using concept of generalized functions [27] and the fundamental solution [14] $G(\lambda, t) = \chi(t)\lambda^{-1} \sin \lambda t$ of the operator $D(\lambda) \equiv [\partial_t^2 + \lambda^2]$ (see passage from (11) to (13) for more details):

$$\begin{aligned}
 \tilde{w}_{n2}(\omega, t) = \frac{2}{\pi\omega^2\sqrt{L_2}} & \left[w_{n2}(L_2, t) - \int_0^t \cos[\omega(t - \tau)] \partial_\tau w_{n2}(L, \tau) d\tau \right]; \\
 \omega \geq 0, \quad t \geq 0. & \quad (37)
 \end{aligned}$$

Taking into account the value of integral [30]

$$\int_0^\infty \frac{J_\gamma(\omega L_2) N_\gamma(\omega r) - N_\gamma(\omega L_2) J_\gamma(\omega r)}{\omega [J_\gamma^2(\omega L_2) + N_\gamma^2(\omega L_2)]} d\omega = \frac{\pi}{2} \left(\frac{L_2}{r}\right)^\gamma; \quad L_2 < r,$$

and applying the inverse transform of (34) to (37), one obtains

$$\begin{aligned}
 w_{n2}(r, t) = & \left(\frac{L_2}{r}\right)^{\gamma-1/2} w_{n2}(L_2, t) \\
 & - \frac{2}{\pi} \sqrt{\frac{r}{L_2}} \int_0^t F_\gamma(r, L_2, t-\tau) \partial_\tau w_{n2}(L_2, \tau) d\tau; \quad r > L_2, \quad (38) \\
 F_\gamma(r, L_2, t-\tau) = & \int_0^\infty \frac{\cos(\omega(t-\tau)) [J_\gamma(\omega L_2) N_\gamma(\omega r) - N_\gamma(\omega L_2) J_\gamma(\omega r)]}{\omega [J_\gamma^2(\omega L_2) + N_\gamma^2(\omega L_2)]} d\omega. \quad (39)
 \end{aligned}$$

For effective numerical implementation of (38), an easy way to compute functions $F_\gamma(r, L_2, t - \tau)$ must be found. Consider the

following function:

$$\begin{aligned}
 & \tilde{F}_\gamma(r, L_2, t - \tau) \\
 &= \frac{1}{2} \left\{ \int_{-\infty}^{\infty} \frac{H_\gamma^{(1)}(zr)}{H_\gamma^{(1)}(zL_2)} \frac{\exp[iz(t-\tau)]}{z} dz + \int_{-\infty}^{\infty} \frac{H_\gamma^{(1)}(zr)}{H_\gamma^{(1)}(zL_2)} \frac{\exp[-iz(t-\tau)]}{z} dz \right\} \\
 &= \int_{-\infty}^{-\delta} \frac{H_\gamma^{(1)}(zr)}{H_\gamma^{(1)}(zL_2)} \frac{\cos[z(t-\tau)]}{z} dz + \int_{\delta}^{\infty} \frac{H_\gamma^{(1)}(zr)}{H_\gamma^{(1)}(zL_2)} \frac{\cos[z(t-\tau)]}{z} dz \\
 &+ \int_{C_\delta} \frac{H_\gamma^{(1)}(zr)}{H_\gamma^{(1)}(zL_2)} \frac{\cos[z(t-\tau)]}{z} dz = - \int_{\delta}^{\infty} \frac{H_\gamma^{(1)}(e^{i\pi}zr)}{H_\gamma^{(1)}(e^{i\pi}zL_2)} \frac{\cos[z(t-\tau)]}{z} dz \\
 &+ \int_{\delta}^{\infty} \frac{H_\gamma^{(1)}(zr)}{H_\gamma^{(1)}(zL_2)} \frac{\cos[z(t-\tau)]}{z} dz - \pi i \left(\frac{L_2}{r} \right)^\gamma \\
 &= 2iF_\gamma(r, L_2, t - \tau) - \pi i \left(\frac{L_2}{r} \right)^\gamma \tag{40}
 \end{aligned}$$

Here $H_\gamma^{(1)}(\cdot)$ is Hankel function of the first kind; C_δ is a semicircle of infinitely small radius δ in the upper half-plane of complex variable z . This semicircle serves as a part of path of integration to detour singularity at $z = 0$. The last passage in (40) was made taking into account (39) and using the following equality [30]:

$$\frac{H_\gamma^{(1)}(zr)}{H_\gamma^{(1)}(zL_2)} - \frac{H_\gamma^{(1)}(e^{i\pi}zr)}{H_\gamma^{(1)}(e^{i\pi}zL_2)} = 2i \frac{J_\gamma(zL_2)N_\gamma(zr) - N_\gamma(zL_2)J_\gamma(zr)}{J_\gamma^2(zL_2) + N_\gamma^2(zL_2)}.$$

The standard technique based on the Cauchy theorem and the Jordan lemma [31] is utilized to compute integrals in curly brackets in the expression (40). As relationship $H_\gamma^{(1)}(zr)/H_\gamma^{(1)}(zL_2) \approx (L_2/r)^{1/2} \exp[iz(r-L_2)]$ is true for $|zL_2| \geq \gamma$ and $z \rightarrow \infty$ [28], then it is possible to close the integration contour by a circular arc of infinitely large radius in the upper half-plane of complex variable z when $r - L_2 > t - \tau$. If $r - L_2 < t - \tau$, then the contour of the first integral is closed in the upper half-plane, and the contour of the second integral is closed in the lower half-plane. Taking into account that all the singularities of the function $H_\gamma^{(1)}(zr)/H_\gamma^{(1)}(zL_2)$ are nothing more than just a finite number of simple poles at points $z = z_s : \text{Im}z_s < 0; s = 1, 2, \dots, n$ which coincide with zeros of the function $H_\gamma^{(1)}(zL_2)$ [32], and taking into account that asymptotic

equality $H_\gamma^{(1)}(zr)/H_\gamma^{(1)}(zL_2) \approx (L_2/r)^\gamma$ is satisfied when $z \rightarrow 0$, and that $\partial_z H_\gamma^{(1)}(zL_2) = L_2 \left[H_{\gamma-1}^{(1)}(zL_2) - \gamma H_\gamma^{(1)}(zL_2) / (zL_2) \right]$, one derive:

$$\begin{aligned} & \tilde{F}_\gamma(r, L_2, t - \tau) \\ &= \begin{cases} -\pi i \left[\left(\frac{L_2}{r} \right)^\gamma + \sum_s \frac{H_\gamma^{(1)}(z_s r)}{H_{\gamma-1}^{(1)}(z_s L_2)} \frac{\exp[-iz_s(t-\tau)]}{z_s L_2} \right]; \tau < t - (r - L_2) \\ 0; \tau > t - (r - L_2) \end{cases}. \end{aligned} \tag{41}$$

Finally, substituting (41) into (40) provides

$$\begin{aligned} & F_\gamma(r, L_2, t - \tau) \\ &= \begin{cases} -\frac{\pi}{2} \sum_s \frac{H_\gamma^{(1)}(z_s r)}{H_{\gamma-1}^{(1)}(z_s L_2)} \frac{\exp[-iz_s(t-\tau)]}{z_s L_2} = -\frac{\pi}{2} S_\gamma(r, L_2, t - \tau); \tau < t - (r - L_2) \\ \frac{\pi}{2} \left(\frac{L_2}{r} \right)^\gamma; \tau > t - (r - L_2) \end{cases}. \end{aligned} \tag{42}$$

Substituting (42) into (38) yields

$$\begin{aligned} w_{n2}(r, t) &= \left(\frac{L_2}{r} \right)^n w_{n2}(L_2, t - (r - L_2)) \\ &+ \sqrt{\frac{r}{L_2}} \int_0^{t-(r-L_2)} S_{n+1/2}(r, L_2, t - \tau) \partial_\tau w_{n2}(L_2, \tau) d\tau; r > L_2, t \geq 0. \end{aligned} \tag{43}$$

Like (14), (43) defines the transport operator, and everything stated above concerning (14) is also true for (43).

The EAC for the total field $U(g, t)$ is obtained from (43) using (6b), (7b), taking into account orthonormality of the transverse functions $\mu_{n2}(\cos \vartheta)$, and keeping in mind that $w_{n2}(r, t) = r u_{n2}(r, t)$:

$$\begin{aligned} U(g, t) &= \sum_n \left\{ \left(\frac{L_2}{r} \right)^{n+1} \int_0^{\pi/2} U(L_2, \tilde{\vartheta}, t - (r - L_2)) \mu_{n2}(\cos \tilde{\vartheta}) \sin \tilde{\vartheta} d\tilde{\vartheta} \right. \\ &+ \sqrt{\frac{L_2}{r}} \int_0^{t-(r-L_2)} S_{n+1/2}(r, L_2, t - \tau) \\ &\times \left. \left[\int_0^{\pi/2} \partial_\tau U(L_2, \tilde{\vartheta}, \tau) \mu_{n2}(\cos \tilde{\vartheta}) \sin \tilde{\vartheta} d\tilde{\vartheta} \right] d\tau \right\} \mu_{n2}(\cos \vartheta); \\ g &= \{r; \vartheta\} \in \mathbf{II}, t \geq 0. \end{aligned} \tag{44}$$

The EAC (44) is nonlocal. It should also be noted here that it does not contain radial derivatives of $U(g, t)$, so it can be implemented on a rectangular grid of coordinates $\{\rho, z\}$ with minimal numerical inaccuracy.

2.2.4. Virtual Feeding Waveguide Concept

The EAC (44) is derived for the semispherical virtual boundary \mathbf{L}_2 , but it can be extended for a spherical boundary which fully surrounds the structure under study [14] (Fig. 2). In such cases, an excitation of the structure is not trivial since in the above formulation of EACs the sources are assumed to be outside the domain \mathbf{Q}_L and physical feeding structures are not allowed to penetrate through the virtual boundary \mathbf{L}_2 . To overcome this problem, a “virtual” feeding waveguide is used to excite the structure. This concept is based on the fact that (5) can be extended to the case of \mathbf{I} being bounded and the conclusion that $U_1^s(g, t)$ is an outgoing wave. In this case, EACs (16) or (25) on the virtual boundary \mathbf{L}_1 reduce the domain of analysis to \mathbf{Q}_L as usual, but \mathbf{I} becomes a “virtually infinite” but physically bounded feeding waveguide. This concept makes the modeling of realistic structures considerable easier, but does not affect the derivation and implementation of the EACs. An example of these structures is presented in Fig. 2: a compact radiator residing in free space is fully surrounded by the spherical virtual boundary \mathbf{L}_2 . The radiator has no flange, as opposed to the radiator with an infinite flange shown in Fig. 1(b); but it can still be excited in the same way using the virtual waveguide \mathbf{I} .

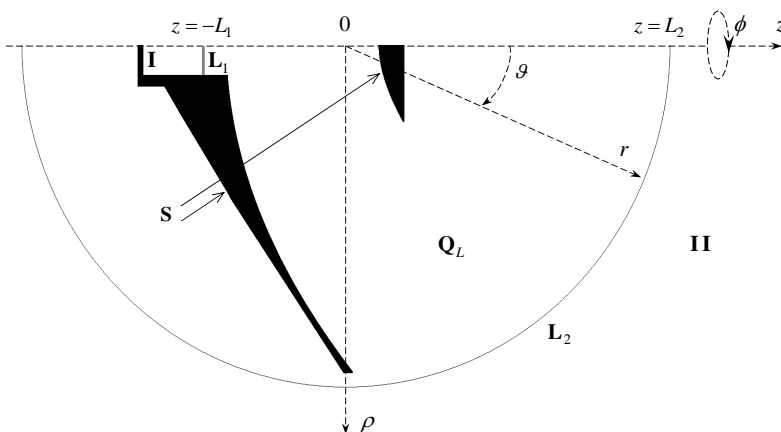


Figure 2. Geometry of a compact radiator without flange.

2.2.5. Conclusion of the Derivations

The result of the derivations presented in Sections 2.1 and 2.2 can be summarized as follows:

Statement: Consider the following problem

$$\begin{aligned} & [-\varepsilon_r(g) \partial_t^2 - P + \partial_z^2 + \partial_\rho (\rho^{-1} \partial_\rho \rho)] U(g, t) = 0; t > 0, g = \{\rho, z\} \in \mathbf{Q}_L \\ & U(g, 0) = 0, \partial_t U(g, t)|_{t=0} = 0; g \in \overline{\mathbf{Q}_L} \\ & D_1 [U(g, t) - U^i(g, t)]|_{g \in \mathbf{L}_1} = 0, D_2 [U(g, t)]|_{g \in \mathbf{L}_2} = 0 \\ & E_{tg}(g, t) = 0, g \in \mathbf{S}; U(0, z, t) = 0; t \geq 0 \end{aligned} \quad (45)$$

where operator $D_1[\cdot]$ is defined by EAC (16) or (25) and operator $D_2[\cdot]$ is defined by EAC (18) or (26) and (44) for waveguide units and radiators, respectively. Then problems (1) and (45) are equivalent in the bounded subdomain \mathbf{Q}_L of the unbounded domain \mathbf{Q} ; the requirements for the uniqueness of the solutions of problems (1) and (45) are identical. It should again be emphasized here that (16), (18), (25), (26), and (44) are exact; replacing problem (1) with problem (45) does not increase the computational error or distort the process of numerical solution.

2.3. Numerical Implementation and FFT-based Acceleration

This section first details the numerical implementation of the EACs (16), (18) and (25), (26). Utilization peculiarities and numerical implementation of an EAC similar to (44) is discussed in [14]. Description of the numerical implementation is followed by an analysis of the computational complexity of the local and nonlocal EACs. The section ends with description of the FFT-based algorithm, which is used for accelerating the pertinent temporal convolutions in the nonlocal EACs (16), (18) and (44).

Using standard FDTD approximation [4] on a uniform rectangular space-time grid, associated with coordinates $\{\rho, z\}$ and time t , for discretization of the problem (45), an explicit computational scheme that updates the uniquely defined grid function $U(j, k, m) \approx U(\rho_j, z_k, t_m)$ is obtained. Here $\rho_j = j\bar{h}$, $z_k = k\bar{h}$, and $t_m = m\bar{l}$; \bar{h} is the space increment (space step) in the ρ and z coordinate directions; and \bar{l} is the time increment (time step). The range of integers $j = 0, 1, \dots, J$, $k = 0, 1, \dots, K$, and $m = 0, 1, \dots, M$ depends on the size of domain \mathbf{Q}_L and the length of the observation time T : $\{\rho_j, z_k\} \in \overline{\mathbf{Q}_L}$ and $0 = t_0 \leq t_m \leq t_M = T$. It should be noted that $-L_1 = z_0 \leq z_k \leq z_K = L_2$ but the boundaries for

ρ_j change depending on the type of the structure. It is assumed that the Courant stability condition between \bar{h} and \bar{l} [4] and the condition, which enforces the uniform boundedness of the approximate solution $U(j, k, m)$ with decreasing \bar{h} and \bar{l} (formula (1.50) in [14]), are satisfied. Under these conditions, the FDTD scheme is stable, and the grid function $U(j, k, m)$ converges to the solution $U(\rho_j, z_k, t_m)$ of the original problem (1). The approximation error is $O(\bar{h}^2)$, but could be improved for example using higher order schemes [33]. In order to achieve the desired second-order accuracy, all integrals are computed using the composite trapezoid rule and all one-sided first-order derivatives are approximated using the second-order one-sided finite differences [34].

2.3.1. Discretization of Nonlocal EACs (16) and (18)

Here the discretization of the EAC (16) on the virtual boundary \mathbf{L}_1 is derived first. The discretization of the EAC (18) on \mathbf{L}_2 can be done in a similar way. In a conventional FDTD scheme, it is more convenient to discretize (15) for the amplitudes $u_{n1}(z, t)$ and then use (2) to obtain boundary values of the total field $U(\rho, -L_1, t)$ rather than to discretize (16) directly. On \mathbf{L}_1 the total field is a sum of the scattered field and the incident wave: $U(\rho, z, t) = U^s(\rho, z, t) + U^i(\rho, z, t)$, and one should remember that (16) is formulated for the scattered field and the problem (45) is being solved for the total field. It is assumed that (2) and (3) are valid two space steps away from the boundary \mathbf{L}_1 into the domain \mathbf{Q}_L . Keeping in mind that $u_{n1}(z, t) = u_{n1}^t(z, t) - v_{n1}(z, t)$, using the composite trapezoid rule to integrate over τ and the second-order one-sided finite differences to calculate the derivative with respect to z , taking into account that $U(\rho, -L_1, 0) = 0$ and $J_0(0) = 1$, and gathering all terms at the $(m + 1)$ -th time step, (15) is discretized:

$$\begin{aligned}
 u_{n1}^t(0, m+1) &= [4u_{n1}^t(1, m+1) - u_{n1}^t(2, m+1) + 4\bar{h}v_{n1}(0, m+1)]/l \\
 &- 2\bar{h} \partial_z v_{n1}(z, m+1)|_{z=-L_1} - 2 \sum_{q=1}^m (J_0(\lambda_{n1}t_{m+1-q}) \\
 &\times [3u_{n1}^t(0, q) - 4u_{n1}^t(1, q) + u_{n1}^t(2, q) + 2\bar{h}\partial_z v_{n1}(z, q)|_{z=-L_1}])\bar{l}/(4\bar{h} + 3\bar{l}). \quad (46)
 \end{aligned}$$

Here $z_0 = -L_1$, and $u_{n1}^t(k, m) \approx u_{n1}^t(z_k, t_m)$ and $v_{n1}(k, m) \approx v_{n1}(z_k, t_m)$ are the grid functions corresponding to the amplitudes $u_{n1}^t(z, t)$ and $v_{n1}(z, t)$, respectively. The values of the total field at

the boundary points, $U(j, 0, m + 1)$, are obtained using (2c):

$$U(j, 0, m + 1) = \sum_n \mu_{n1}(\rho_j) u_{n1}^t(0, m + 1), \quad b_1 \leq \rho_j \leq a_1,$$

$$n = \begin{cases} 1, 2, \dots, N^{g,w}; & TE_{0n} \text{ waves} \\ 0, 1, \dots, N^{g,w}; & TM_{0n} \text{ waves} \end{cases} \quad (47)$$

Here $N^{g,w}$ is the number of the modes taken into account. Together (46) and (47) are the discretization of the EAC (16). In (46), $\partial_z v_{n1}(z, m + 1)|_{z=-L_1}$ are computed from

$$v_{n1}(0, m + 1) = -\bar{l} \sum_{q=1}^m (J_0(\lambda_{n1} t_{m+1-q}) \partial_z v_{n1}(z, q)|_{z=z_0}) - \frac{\bar{l}}{2} \partial_z v_{n1}(z, m + 1)|_{z=z_0} \quad (48)$$

which is obtained by discretizing (17).

Discretized EACs are integrated in the FDTD scheme in the following way:

- i. At the time step m the FDTD routine computes the total field values at all inner points of the grid, $U(j, k, m + 1)$.
- ii. The values of the spatio-temporal amplitudes at the points adjacent to the virtual boundary \mathbf{L}_1 , $u_{n1}^t(1, m + 1)$ and $u_{n1}^t(2, m + 1)$ ($z_1 = -L_1 + \bar{h}$ and $z_2 = -L_1 + 2\bar{h}$), are computed using (3).
- iii. The values of the spatio-temporal amplitudes at the boundary points, $u_{n1}^t(0, m + 1)$ ($z_0 = -L_1$), are computed using (46), and saved for the future use.
- iv. The values of the total field at the boundary points, $U(j, 0, m + 1)$, are reconstructed from $u_{n1}^t(0, m + 1)$ using (47). Then proceed to the next time step.

The EAC (18) on the virtual boundary \mathbf{L}_2 is discretized and integrated in the FDTD scheme similarly; but one should remember that on this boundary $U^i(\rho, z, t) = 0$ and $U(\rho, z, t) = U^s(\rho, z, t)$.

2.3.2. Discretization of Local EACs (25) and (26)

Here the discretization of the EAC (25) on the virtual boundary \mathbf{L}_1 is derived first. The discretization of the EAC (26) on \mathbf{L}_2 can be done in a similar way. On \mathbf{L}_1 the total field is a sum of the scattered field and the incident wave: $U(\rho, z, t) = U^s(\rho, z, t) + U^i(\rho, z, t)$, and one should remember that (25) is formulated for the scattered field and

the problem (45) is being solved for the total field. Approximating the derivatives in the left side of the auxiliary initial-boundary value problem in (25) with the central differences, and using the second-order one-sided differences to approximate the derivatives in the right-hand side, an explicit three-step scheme that updates the grid function $W_1(j, m, n) \approx W_1(\rho_j, t_m, \varphi_n)$; $n = 0, 1, \dots, N^\varphi$, $\varphi_n = n\pi/2N^\varphi$, is obtained:

$$\begin{aligned}
 W_1(j, m+1, n) &= A_{j,n}^+ W_1(j+1, m, n) + A_{j,n}^- W_1(j-1, m, n) \\
 &+ A_{j,n}^0 W_1(j, m, n) - W_1(j, m-1, n) \\
 &- \frac{\bar{l}^2}{2\bar{h}}(3U(j, 0, m) - 4U(j, 1, m) + U(j, 2, m)) + \partial_z U^i(j, z, m)|_{z=z_0}; \\
 b_1 &< \rho_j < a_1, j(b_1) = 0 < j < J = j(a_1), J = a_1/\bar{h}, 0 < m \leq M \\
 W_1(j, 0, n) &= W_1(j, 1, n) = 0, z_0 = -L_1, z_1 = -L_1 + \bar{h} \\
 TE_{0n} : W_1(0, m, n) &= W_1(J, m, n) = 0
 \end{aligned} \tag{49}$$

$$\begin{aligned}
 TM_{0n} : W_1(0, m, n) &= \frac{b_1}{b_1 + \bar{h}} W_1(1, m, n), \\
 W_1(J, m, n) &= \frac{a_1}{a_1 + \bar{h}} W_1(J-1, m, n).
 \end{aligned}$$

Here $A_{j,n}^\pm = \bar{l}^2 \sin^2 \varphi_n (2\rho_j \pm \bar{h}) / (2\rho_j \bar{h})$, $A_{j,n}^0 = 2 - \bar{l}^2 \sin^2 \varphi_n (2\rho_j^2 + \bar{h}^2) / (\rho_j^2 \bar{h}^2)$, and $\partial_z U^i(j, z, m)|_{z=z_0} \approx \partial_z U^i(\rho_j, z, t_m)|_{z=z_0}$ is the grid function corresponding to $\partial_z U^i(\rho, z, t)$. The time derivative of $W_1(j, m, n)$ is approximated using the second-order one-sided difference:

$$\partial_t W_1(j, t, n)|_{t=t_{m+1}} \approx \frac{3W_1(j, m+1, n) - 4W_1(j, m, n) + W_1(j, m-1, n)}{2\bar{t}}. \tag{50}$$

The values of the total field at the boundary points, $U(j, 0, m+1)$, are obtained integrating (50) with respect to φ using any numerical integration method that can provide the required accuracy. It is clear that $W_1(j, m+1, n)$, $W_1(j, m, n)$, and $W_1(j, m-1, n)$ should be stored in the memory.

The Equation (17) (or to be more precise, its discrete version (48)) is utilized for precomputation of the concerted values of the amplitudes of the incident wave and its derivative. As the whole field rather than its amplitudes is utilized in the discretization of the local EAC (25), the incident wave and its derivative are reconstructed from their amplitudes using (2a).

(49) and (50) are integrated in the FDTD scheme in the following way:

- i. At the time step m the FDTD routine computes the total field values at all inner points of the grid, $U(j, k, m+1)$.

- ii. The values of the auxiliary variable, $W_1(j, m + 1, n)$, are computed using (49).
- iii. The time derivative of the auxiliary variable with respect to time, $\partial_t W_1(j, t, n)|_{t=t_{m+1}}$, is computed using (50).
- iv. The values of the total field at the boundary points, $U(j, 0, m + 1)$, are computed by numerically integrating of the time derivatives obtained at step (iii). Then proceed to the next time step.

The EAC (26) on the virtual boundary \mathbf{L}_2 is discretized and integrated in the FDTD scheme similarly; but one should remember that on this boundary $U^i(\rho, z, t) = 0$ and $U(\rho, z, t) = U^s(\rho, z, t)$.

2.3.3. Computational Complexity

Obviously, the computational complexity of the FDTD-based solution of (45) depends on the type (nonlocal or local) of the EACs being discretized. In what follows, the computational complexity of the solution is derived for the most general case, namely, an open radiating end of a coaxial waveguide with an elongated central conductor over an infinite perfectly conducting plane (Fig. 3). This example includes both a local/nonlocal EAC on the planar boundary \mathbf{L}_1 and a nonlocal EAC on the semispherical boundary \mathbf{L}_2 . If the explicit three-step $O(\bar{h}^2)$ -accurate FDTD scheme [4] is used and the nonlocal EACs (16)

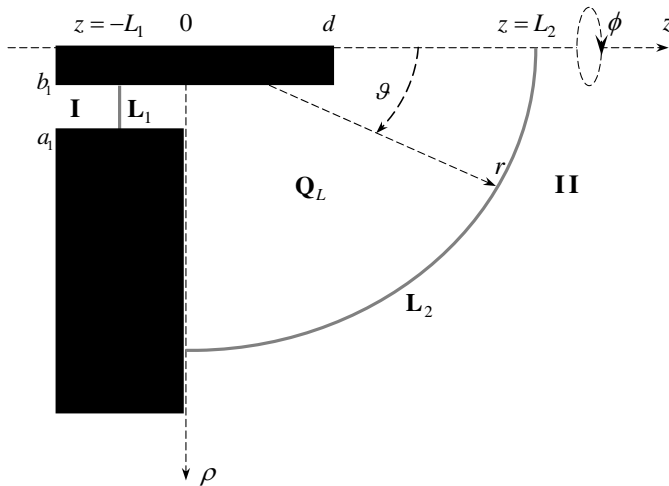


Figure 3. Geometry of the test problem — an open end of coaxial waveguide with elongated central conductor over infinite perfectly conducting plane.

and (44) on \mathbf{L}_1 and \mathbf{L}_2 are discretized as described above, then the total computational cost of the solution can be written as:

$$S \approx \underbrace{O(PM)}_{C_{\text{FDTD}}} + \underbrace{O(N^{g,w}M^2)}_{C_{L_1}^{PR}} + \underbrace{O(N^{g,w}M^2)}_{C_{L_1}^{NL}} + \underbrace{O(N^{g,r}M^2)}_{C_{L_2}^{NL}} \quad (51)$$

Here the terms C_{FDTD} , $C_{L_1}^{PR}$, $C_{L_1}^{NL}$, and $C_{L_2}^{NL}$ represent the computational costs of the FDTD solution, precomputation of the incident field's derivative, and the numerical implementation of the nonlocal EACs on \mathbf{L}_1 and \mathbf{L}_2 , respectively. $C_{L_1}^{PR}$, $C_{L_1}^{NL}$, and $C_{L_2}^{NL}$ are obtained by counting the numbers of additions and multiplications in discrete versions of (17), (16) and (44), respectively. Integers P , M , $N^{g,w}$ and $N^{g,r}$ are the total numbers of the FDTD cells in the domain of computation, the time steps, and the modes taken into account in the discretization of the nonlocal EACs (16) and (44), respectively.

Replacing the nonlocal EAC (16) on the virtual boundary \mathbf{L}_1 with its local equivalent, EAC (25), yields a new estimate for the total computational cost:

$$S \approx \underbrace{O(PM)}_{C_{\text{FDTD}}} + \underbrace{O(N^{g,w}M^2)}_{C_{L_1}^{PR}} + \underbrace{O(N^\varphi M)}_{C_{L_1}^L} + \underbrace{O(N^{g,r}M^2)}_{C_{L_2}^{NL}} \quad (52)$$

In (52), $C_{L_1}^L$ represents the computational cost of the numerical implementation of the local EAC, integer N^φ is the number of points needed to compute the integral over φ in the local EAC (numerical integration of (50)). $C_{L_1}^L$ is obtained by counting the numbers of additions and multiplications in discrete version of (25). Comparing $C_{L_1}^L$ in (52) with $C_{L_1}^{NL}$ in (51), it is clear that for large M utilization of the local EACs might lead to a significant reduction in computational resources provided that $N^{g,w}M \gg N^\varphi$. However, numerical experiments show that this condition may not always be satisfied; to obtain accurate results especially when analyzing resonant wave interactions, N^φ must be very high. In addition, $C_{L_2}^{NL}$ and $C_{L_1}^{PR}$, which are present both in (51) and (52), might dominate the overall computational costs for large M . During the analysis of resonant wave interactions, one can still utilize the nonlocal EACs efficiently provided that the temporal convolutions pertinent to nonlocal conditions are computed fast. To this end, the blocked-FFT based acceleration scheme presented in [16–22] is used here.

The blocked-FFT based acceleration algorithm makes use of the temporal invariance of the convolutions present in the nonlocal EACs (16), (18), and (44). The algorithm is applied to the discretized version of these EACs, where now the temporal convolutions are

$u(5)$ and update $u(6)$, $u(7)$ and $u(8)$. At time step 5, the 1×1 block $J(1)$ multiplies $u(5)$ to yield $u(6)$. At time step 6, the 2×2 block multiplies $[u'(5) \ u'(6)]^T$ yield $u(7)$ and update $u(8)$. At time step 7, the 1×1 block $J(1)$ multiplies $u(7)$ to yield $u(8)$. This block-by-block multiplication scheme is executed until the end of the simulation time t . In this scheme, the multiplication of a matrix block with a vector can be accelerated using FFTs. Consider, for example, the multiplication at time step 4: The result of multiplying the 4×4 block with the column vector $[u'(1) \ u'(2) \ u'(3) \ u'(4)]^T$ is equal to the last four elements of the circular convolution of $J_{in} = \{J(1), J(2), J(3), J(4), J(5), J(6), J(7)\}$ with $u_{in} = \{u'(1), u'(2), u'(3), u'(4), 0, 0, 0\}$. This convolution can be computed exactly using discrete Fourier transforms (DFTs) [35], i.e., computing $DFT^{-1}[DFT[J_{in}]DFT[u_{in}]]$. In this expression, DFTs are replaced with FFTs without any numerical approximation for speed up. Since the large blocks are multiplied less often than the small ones and each block, which bigger than 1×1 , is multiplied using FFTs, the computational complexity of the block-by-block multiplication (i.e., the discrete convolution in (46)) is reduced to $O(M \log^2 M)$ from $O(M^2)$.

Using the FFT-based acceleration technique described above for computing all temporal convolutions pertinent to nonlocal EACs, the computational complexity of the FDTD solution is reduced to

$$\begin{aligned}
 S \approx & \underbrace{O(PM)}_{C_{\text{FDTD}}} + \underbrace{O(N^{g,w} M \log^2 M)}_{C_{L_1}^{PR,FFT}} + \underbrace{O(N^{g,w} M \log^2 M)}_{C_{L_1}^{NL,FFT}} \\
 & + \underbrace{O(N^{g,r} M \log^2 M)}_{C_{L_2}^{NL,FFT}} \tag{55}
 \end{aligned}$$

Comparing (55) with (51) one concludes that $C_{L_1}^{NL,FFT} \ll C_{L_1}^{NL}$, $C_{L_2}^{NL,FFT} \ll C_{L_2}^{NL}$, and $C_{L_1}^{PR,FFT} \ll C_{L_1}^{PR}$ especially for large M . This results in significant savings in computational resources. Comparing (55) with (52), one can conclude that that for $C_{L_1}^{NL,FFT} < C_{L_1}^L$, $N^{g,w} \log^2 M < N^\varphi$ should be satisfied. This is possible to achieve for resonant structures where N^φ is very large.

Looking at the comparisons provided above, one can conclude the following: (i) The implementation of EACs on spherical boundaries should always be accelerated using the blocked-FFT based algorithm. (ii) The precomputation of the incident field's derivative on virtual boundaries should always be accelerated using the blocked-FFT based algorithm. (iii) The implementation of nonlocal EACs on planar

boundaries can be accelerated using the blocked-FFT based algorithm or localization. One can compare $N^{g,w} \log^2 M$ and N^φ to see which one will be more efficient. It should be emphasized here again that neither blocked-FFT based algorithm nor localization introduces additional numerical errors. Both of these methods are exact.

3. NUMERICAL RESULTS

This section presents numerical results that demonstrate the efficiency and accuracy of the blocked-FFT accelerated FDTD scheme with nonlocal/local EACs detailed in this paper. Since the accuracy of EACs has been the subject of several other publications (see [14] for example), the emphasis here is on the accuracy and efficiency of the blocked-FFT acceleration. Two different examples are considered. Both examples are run on a workstation with a 2.67 GHz Xeon CPU and 23.4 GB of RAM.

3.1. Efficiency of the Blocked-FFT Based Acceleration Scheme

In the first example, the computational complexity estimates for $C_{L_1}^{PR,FFT}$ and $C_{L_1}^{PR}$ are verified and compared (without the FDTD grid). To this end, a planar virtual boundary in the cross-section of a coaxial waveguide with the outer conductor radius $a_1 = 1.5$ and the inner conductor radius $b_1 = 0.9$ is considered and (17) is computed on this boundary (to be more precise, its discrete version (48)). The space step is $\bar{h} = 0.01$, and the time step is $\bar{l} = 0.005$. The number of modes used for expanding the field is $N^{g,w} = 6$, the number of grid cells used for discretizing the boundary is $J^w = 61$. Fig. 4(a) presents the CPU times required by the blocked-FFT accelerated and non-accelerated computation while the number of time steps, M , is changed from 1000 to 2 000 000. As clearly shown in the figure, theoretical estimates of the computational complexity are in good agreement with numerical experiment results. Also, figure clearly shows that blocked-FFT accelerated computation becomes undoubtedly faster than non-accelerated computation when $M > 4000$.

3.2. Efficiency and Accuracy of the Blocked-FFT Based Accelerated FDTD Scheme

The second example is designed to demonstrate the efficiency and accuracy of the blocked-FFT accelerated FDTD scheme. For this purpose, the same radiator, which was used as an example in the

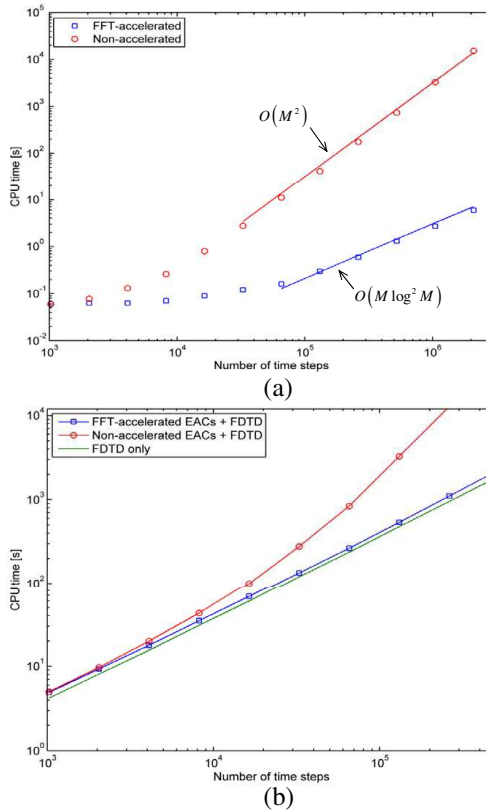


Figure 4. CPU times versus number of time steps: (a) Comparison of CPU times for FFT-accelerated and nonaccelerated EACs. (b) Comparison of total CPU times for FDTD schemes with FFT-accelerated and nonaccelerated EACs and only FDTD updates for the radiator problem.

previous section to derive the computational complexity estimates is considered (see Fig. 3). The feeding structure is a coaxial waveguide with the outer conductor radius $a_1 = 1$ and the inner conductor radius $b_1 = 0.3$, the length of the elongated central conductor is $d = 1.57$. The space step is $\bar{h} = 0.02$, and the time step is $\bar{l} = 0.01$. The structure is excited by a quasi-monochromatic signal $v_{01}(0, t) = \cos(ft)$, where $f = 7.5$ is the central frequency. The virtual boundaries (planar) \mathbf{L}_1 and (spherical) \mathbf{L}_2 are located at $z = -L_1 = -1$ and $r = L_2 = 8$, respectively. \mathbf{L}_1 is discretized using $J^w = 36$ grid cells, and the field on \mathbf{L}_1 is expanded using $N^{g,w} = 5$ modes. \mathbf{L}_2 is discretized using

$J^r = 565$ arc segments and the field on \mathbf{L}_2 is expanded using $N^{g,r} = 30$ modes. The total number of grid cells in the computation domain \mathbf{Q}_L is $P = 127350$.

Figure 4(b) presents the CPU times required by the FDTD scheme with blocked-FFT accelerated EACs (see (55) for the computational complexity estimate), FDTD scheme with non-accelerated EACs (see (51) for the computational complexity estimate), and the FDTD scheme itself (only the FDTD updates) while the number of time steps, M , is changed from 1000 to 500 000. Fig. 4(b) clearly demonstrates the efficiency of the blocked-FFT accelerated FDTD scheme.

To demonstrate that the blocked-FFT acceleration introduces only numerical noise in the solution, the H_ϕ component computed at $\{\rho = 95; z = 270\}$ by the FFT-accelerated and non-accelerated FDTD schemes are compared in Fig. 5. For this simulation the same structure as in the previous one is utilized. $M = 8000$ and the structure is excited by a pulse $v_{01}(0, t) = \cos[f(t - \tilde{T})] \sin[\Delta f(t - \tilde{T})] / (t - \tilde{T})$, here $f = 7.5$ is the central frequency, Δf is the bandwidth, and $\tilde{T} = 30$ is the delay. As expected the difference between two results is on the level of 10^{-13} , which is far below the error of the FDTD discretization scheme. For the sake of completeness, for this simulation, snapshots of the H_ϕ component computed at times $t = 33$, $t = 35$, $t = 39$, and $t = 40$ on the whole computation domain \mathbf{Q}_L are presented in Figs. 6(a), (b), (c), and (d), respectively.

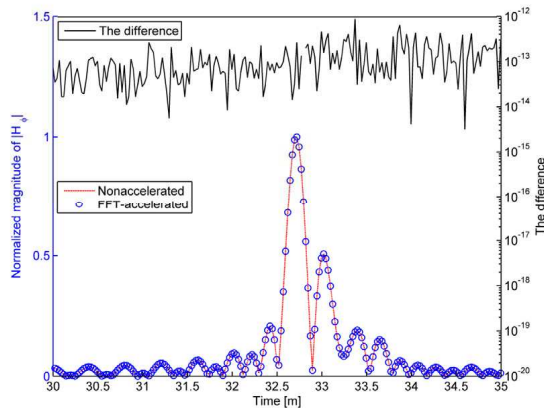


Figure 5. Comparison of the normalized magnitude of $|H_\phi|$ computed at the observation point using FDTD schemes with FFT-accelerated and non-accelerated EACs.

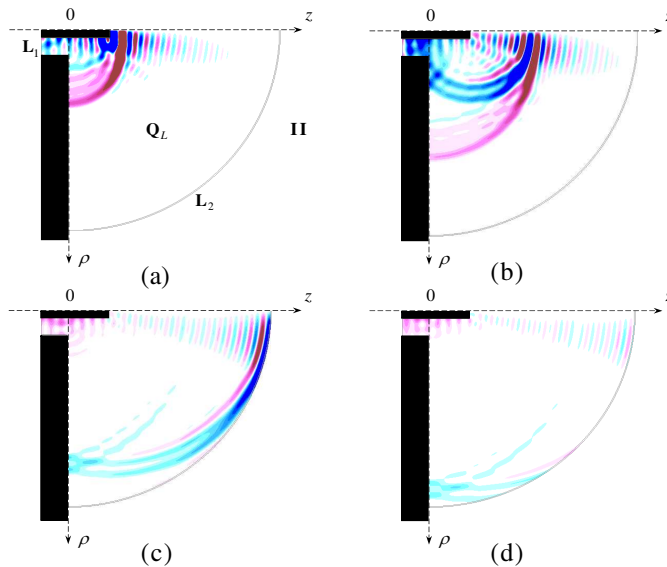


Figure 6. H_ϕ pattern: (a) $t = 33$ — the pulse is leaving the radiator. (b) $t = 35$ — the pulse is propagating freely. (c) $t = 39$ — the pulse is crossing the virtual boundary. (d) $t = 40$ — the pulse has just crossed the boundary without reflection.

4. CONCLUSIONS AND FUTURE RESEARCH DIRECTIONS

An accurate and efficient method for transient analysis of wave interactions on axially symmetric structures is presented. The pillars of the method are the nonlocal/local EACs and the blocked-FFT based acceleration scheme. Being imposed on the virtual boundaries, the EACs allow reduction of unbounded physical domain of interest to a bounded computation domain without loss of exactness. Spatially and temporally nonlocal EACs are derived on the planar boundaries inside the regular waveguides and on the semispherical boundary in the open space. Localization technique is applied to the EACs imposed on planar boundaries to reduce the computational resources required. When localization is not possible or inefficient, the presented blocked-FFT based scheme is used to accelerate the computation of the temporal convolutions present in the nonlocal EACs. Both localization and blocked-FFT acceleration schemes are numerically exact.

The method presented in this paper is a novel and efficient approach to reliable transient analysis of wave interactions on resonant

structures. Methods capable of accurate and efficient characterization of long-duration field interactions on such structures are indispensable for analysis and synthesis of microwave energy compressors and radiators of high-power short radio pulses. Several problems involving the design of microwave energy compressors and radiators will be studied in the subsequent papers.

REFERENCES

1. Kuzmitchev, I. K., P. M. Melezhyk, V. L. Pazynin, K. Y. Sirenko, Y. K. Sirenko, O. S. Shafalyuk, and L. G. Velychko, "Model synthesis of energy compressors," *Radiophysics and Electronics: Sci. Works Collection*, Vol. 13, No. 2, 166–172, NAS of Ukraine, A. Usikov Institute of Radiophysics and Electronics, Kharkiv, 2008.
2. Tantawi, S. G., R. D. Ruth, A. E. Vlieks, and M. Zolotarev, "Active high-power RF pulse compression using optically switched resonant delay lines," *IEEE Trans. Microwave Theory Tech.*, Vol. 45, No. 8, 1486–1492, 1997.
3. Vikharev, A. L., A. M. Gorbachev, O. A. Ivanov, V. A. Isaev, S. V. Kuzikov, B. Z. Movshevich, J. Hirshfield, and S. H. Gold, "Active Bragg compressor of 3-cm wavelength microwave pulses," *Radiophys. Quantum Electron.*, Vol. 51, No. 7, 539–555, 2008.
4. Taflove, A. and S. C. Hagness, *Computational Electrodynamics: The Finite-Difference Time-Domain Method*, Artech House, Boston, 2005.
5. Keller, J. B., "Exact non-reflecting boundary conditions," *J. Comput. Phys.*, Vol. 82, 172–192, 1989.
6. Hagstrom, T., "Radiation boundary conditions for the numerical simulation of waves," *Acta Numerica*, Vol. 8, 47–106, 1999.
7. Olivier, J. C., "On the synthesis of exact free space absorbing boundary conditions for the finite-difference time-domain method," *IEEE Trans. Antennas Propag.*, Vol. 40, No. 4, 456–460, 1992.
8. De Moerloose, J. and D. De Zutter, "Surface integral representation radiation boundary condition for the FDTD method," *IEEE Trans. Antennas Propag.*, Vol. 41, No. 7, 890–896, 1993.
9. Ziolkowski, R. W., N. K. Madsen, and R. C. Carpenter, "Three-dimensional computer modeling of electromagnetic fields: A global lookback lattice truncation scheme," *J. Comput. Phys.*, Vol. 50, 360–408, 1983.
10. Hagstrom, T. and H. B. Keller, "Exact boundary conditions at an

- artificial boundary for partial differential equations in cylinders,” *SIAM J. Math. Anal.*, Vol. 17, No. 2, 322–341, 1986.
11. Grote, M. J. and J. B. Keller, “Nonreflecting boundary conditions for Maxwell’s equations,” *J. Comput. Phys.*, Vol. 139, 327–342, 1998.
 12. Lubich, C. and A. Shadle, “Fast convolution for nonreflecting boundary conditions,” *SIAM J. Sci. Comput.*, Vol. 24, No. 1, 161–182, 2002.
 13. Alpert, B., L. Greengard, and T. Hagstrom, “Rapid evaluation of nonreflecting boundary kernels for time-domain wave propagation,” *SIAM J. Numer. Anal.*, Vol. 37, No. 4, 1138–1164, 2000.
 14. Sirenko, Y. K., S. Strom, and N. P. Yashina, *Modeling and Analysis of Transient Processes in Open Resonant Structures — New Methods and Techniques*, Springer, Berlin, 2007.
 15. Sirenko, K. Y. and Y. K. Sirenko, “Exact “absorbing” conditions in the initial boundary-value problems of the theory of open waveguide resonators,” *Comput. Math. Math. Phys.*, Vol. 45, No. 3, 490–506, 2005.
 16. Hairer, E., C. H. Lubich, and M. Schlichte, “Fast numerical solution of nonlinear Volterra convolution equations,” *SIAM J. Sci. Stat. Comput.*, Vol. 6, No. 3, 532–541, 1985.
 17. Yilmaz, A. E., D. S. Weile, B. Shanker, J.-M. Jin, and E. Michielssen, “Fast analysis of transient scattering in lossy media,” *IEEE Antennas Wireless Propag. Lett.*, Vol. 1, No. 1, 14–17, 2002.
 18. Bagci H., A. E. Yilmaz, and E. Michielssen, “A fast hybrid TDIE-FDTD-MNA scheme for analyzing cable-induced transient coupling into shielding enclosures,” *Proc. IEEE Int. Symp. Electromagn. Compat.*, Vol. 3, 828–833, 2005.
 19. Bagci, H., A. E. Yilmaz, V. Lomakin, and E. Michielssen, “Fast solution of mixed-potential time-domain integral equations for half-space environments,” *IEEE Trans. Geosci. Remote Sensing*, Vol. 43, No. 2, 269–279, 2005.
 20. Bagci, H., A. E. Yilmaz, and E. Michielssen, “FFT-accelerated MOT-based solution of time-domain BLT equations,” *Proc. IEEE Int. Antennas Propagat. Symp.*, 1175–1178, 2006.
 21. Bagci, H., A. E. Yilmaz, J.-M. Jin, and E. Michielssen, “Fast and rigorous analysis of EMC/EMI phenomena on electrically large and complex structures loaded with coaxial cables,” *IEEE Trans. Electromagn. Compat.*, Vol. 49, No. 2, 361–381, 2007.
 22. Bagci, H., A. E. Yilmaz, and E. Michielssen, “An FFT-accelerated

- time-domain multiconductor transmission line simulator,” *IEEE Trans. Electromagn. Compat.*, Vol. 52, No. 1, 199–214, 2010.
23. Sirenko, Y. K., L. G. Velychko, and F. Erden, “Time-domain and frequency-domain methods combined in the study of open resonance structures of complex geometry,” *Progress In Electromagnetics Research*, Vol. 44, 57–79, 2004.
 24. Velychko, L. G., Y. K. Sirenko, and O. S. Shafalyuk, “Time-domain analysis of open resonators. Analytical grounds,” *Progress In Electromagnetics Research*, Vol. 61, 1–26, 2006.
 25. Velychko, L. G. and Y. K. Sirenko, “Controlled changes in spectra of open quasi-optical resonators,” *Progress In Electromagnetics Research B*, Vol. 16, 85–105, 2009.
 26. Ladyzhenskaya, O. A., *The Boundary Value Problems of Mathematical Physics*, Springer-Verlag, New York, 1985.
 27. Vladimirov, V. S., *Equations of Mathematical Physics*, Dekker, New York, 1971.
 28. Korn, G. A. and T. M. Korn, *Mathematical Handbook for Scientists and Engineers*, McGraw-Hill, New York, 1961.
 29. Bateman, H. and A. Erdelyi, *Higher Transcendental Functions*, Vol. 2, McGraw-Hill, New York, 1953.
 30. Prudnikov, A. P., Y. A. Brychkov, and O. I. Marichev, *Integrals and Series*, Vol. 2, Gordon and Breach, New York, 1986.
 31. Von Hurwitz, A., *Allgemeine Funktionentheorie und Elliptische Funktionen*, Von Courant, R., *Geometrische Funktionentheorie*, Springer-Verlag, Berlin, 1964 (in German).
 32. Abramowitz, M. and I. A. Stegun, Ed., *Handbook of Mathematical Functions*, Dover, New York, 1972.
 33. Kantartzis, N. V. and T. D. Tsiboukis, *High Order FDTD schemes for Waveguide and Antenna Structures*, Morgan&Claypool, San Rafael, CA, 2006.
 34. Gerald, C. F. and P. O. Wheatley, *Applied Numerical Analysis*, Addison-Wesley, Boston, 1999.
 35. Oppenheim, A. V., R. W. Schaffer, and J. R. Buck, *Discrete-Time Signal Processing*, Prentice-Hall, Englewood Cliffs, NJ, 1999.